In-situ SEM Microrobotics for Versatile Force/Deformation Characterization: Application to Third-Body MoS_2 Wear Particles

Ralf Hannouch, Valentin Reynaud, Guillaume Colas, Jean-Yves Rauch, Joel Agnus, Olivier Lehmann, François Marionnet, Cédric Clevy

In-situ SEM Microrobotics for Versatile Force/Deformation Characterization: Application to Third-Body MoS_2 Wear Particles

Ralf Hannouch[1,2*], Valentin Reynaud[1], Guillaume Colas[1*], Jean-Yves Rauch[1], Joel Agnus[1], Olivier Lehmann[1], François Marionnet[1] and Cédric Clévy[1*]

[1]Univervité de Franche-Comté, SUPMICROTECH-ENSMM, CNRS, FEMTO-ST institute, Besançon, 25000, France.
[2]Joint Masters Degree program in Mechatronic Engineering, EU4M, Oviedo, 33007, Spain.

*Corresponding author(s). E-mail(s): ralf.hannouch@eu4m.eu; guillaume.colas@femto-st.fr; cedric.clevy@femto-st.fr;

Abstract

Purpose: This article explores the challenges and solutions in the physical characterization of materials at the microscale using robotized systems, with a specific focus on manipulating and characterizing micrometer-sized particles with different and complex 3D shapes and internal sub-micrometer structures. In this paper, the studied particles are Molybdenum diSulfide (MoS2) based materials generated within the contact interface during friction.These particles are being studied because they offer a particularly promising solution for reducing mechanical friction and the associated high energy losses. However, they are distributed randomly within the contact area and possess intricate sub-micrometer structures.
Methods: Characterization demands precise manipulation techniques in an in-situ Scanning Electron Microscope(SEM) environment. To address these challenges, existing commercial micro and nanomanipulation tools are integrated within a vacuum SEM chamber, and robotics strategies are investigated to enable the whole process from particle preparation, and manipulation setup definition, to effective MoS_2 particle characterization all in-situ SEM.
Results: A set of several complementary experimental investigations are done and involve force measurement and deformation estimation studies, leading to

the first qualitative results on MoS_2 based particles directly from the friction track. The work contributes to advancements in both microscale manipulation and characterization. It also has implications for lubrication research.

Keywords: microrobotics, in-situ, micromanipulation, categorization, third-body, Molybdenum diSulfide (MoS_2).

1 INTRODUCTION

In recent years, the utilization of robotics within the Scanning Electron Microscope (SEM) environment has garnered significant interest due to its diverse and promising applications in various fields, including nano-electronics, instrumentation, and materials research [1–3]. The ability to perform a sequence of tasks, ranging from sample preparation, separation, and manipulation, to multimodal characterization, under the SEM presents a multitude of opportunities for scientific advancements and technological innovations. Among the compelling applications, the study of the third-body material stands out as an area of interest. Self-created inside the contact interface during friction, the third body drives lubrication and wear performances [4][5]. Reliable characterization of its physical properties offers key information to help reduce friction, one of the most significant sources of energy losses [6]. It also opens up the route to far-reaching implications for future ecological and sustainable solutions.

Understanding and characterizing third-body particles' mechanical properties, including forces and deformations, are compelling, given their relevance in addressing friction-related challenges. Several studies have demonstrated the potential of using nanomanipulation platforms inside a SEM for motion control [7] and multi-physical characterization [8]. Michelson et al. notably succeeded in doing compression tests in-situ SEM useful to demonstrate the superiority of the developed structure [9]. The studied structures are cubes that differ from the ones studied in the present paper. Indeed, the complexity and dimensions of these particles (micrometer-sized non-identical 3D structures) necessitate advanced tools and robotic strategies to achieve a complete sequence of tasks within the SEM environment. Adam et al. [10] also highlighted the importance of considering force sensors and robots together when doing microrobotic-based force sensing while Govillas et al. [11] showed the strong influence of angular imperfections during compression tests. Specific strategies can also be investigated based on accurate force and or position dynamic measurement to succeed in achieving complex tasks at the microscale [12, 13].

In this study, the challenges posed by the manipulation and characterization of these microstructures are not only specific to this study but also extend to numerous other applications. This common problem calls for the development of robust and innovative strategies to facilitate a wide range of tasks in the SEM environment. It is in this context that this article aims to propose an approach to tackle the complexities of manipulating and characterizing micrometer-sized 3D particles, offering insights and solutions applicable across various fields of research.

Through the integration of existing commercial micro and nanomanipulation tools, along with advanced robotic strategies, this study endeavors to shed light on the potential of using robotics for the precise manipulation and analysis of materials with intricate 3D structures. By addressing the challenges of limited workspace, tool selection, and automation, this case study aims to contribute to the broader understanding of the lubrication mechanisms involving solid third-body materials while paving the way for future advancements in microscale materials research, friction studies, and lubricants.

2 MATERIALS and METHODS

2.1 3D microscale particles

The aim of this study is to make it possible to use several in-situ characterization tools sem using the inherent versatility of robots. In order to best demonstrate the capabilities of this approach, the characterization of 3D grains with complex microstructures is considered as a case study, corresponding to numerous applications. In this paper, we especially investigate, as case-study, the characterization of third-body MoS_2 wear particles. MoS2 and MoS2 based materials offer a particularly promising solution for reducing mechanical friction and the associated high energy losses. Better understanding of the wear particles properties may help find new directions towards improving its performances.

This case study focuses on investigating the mechanical properties/response of three distinct types of particles: (i) raw Molybdenum disulfide (MoS_2) grains originating from commercially available powder (Sigma Aldrich), (ii) third bodies generated by friction on pure MoS_2 coating deposited by burnishing commercially available MoS2 powder on steel substrates [14], and (iii) third bodies generated by friction on MoS_2+Tantalum (Ta) coating deposited by PVD deposition technique [15]. These third-body particles are created during friction, and while some are trapped within the contact interface, others are ejected outside, Fig. 1(c). In our specific study, these third bodies are created under ambient air conditions, during the pure sliding test, Fig. 1(a). Pure MoS_2 coating exhibits higher fiction than MoS_2+Ta. MoS_2 started to fail to lubricate around 480 cycles when the substrate started to be exposed leading to a sudden peak of friction. MoS_2+Ta achieved long-lasting lubrication over the 1000 cycles, Fig. 1(b). Friction tracks are covered with third body materials and MoS_2 shows higher ejection of particles around the friction tracks on both the ball and the disc. Fig. 1(c) shows how large the region covered by ejected particles can be as compared to the region in contact with the disc substrate and undergoing friction. The figure also shows that particles exhibit a large range of geometry and sizes. Cutting those particles using FIB can damage the structure and even melt them, coping with the heterogeneity of their geometries is mandatory and a solution must be found to select, manipulate, and characterize them mechanically. That constitutes the main objective of the present study.

Each of these particles exhibits distinct structures, sizes, and morphologies (Fig. 2(b)). Particles originating from pure MoS_2 lubricated contact exhibit a dense and continuous structure while raw MoS_2 particle has an anisotropic lamellar structure

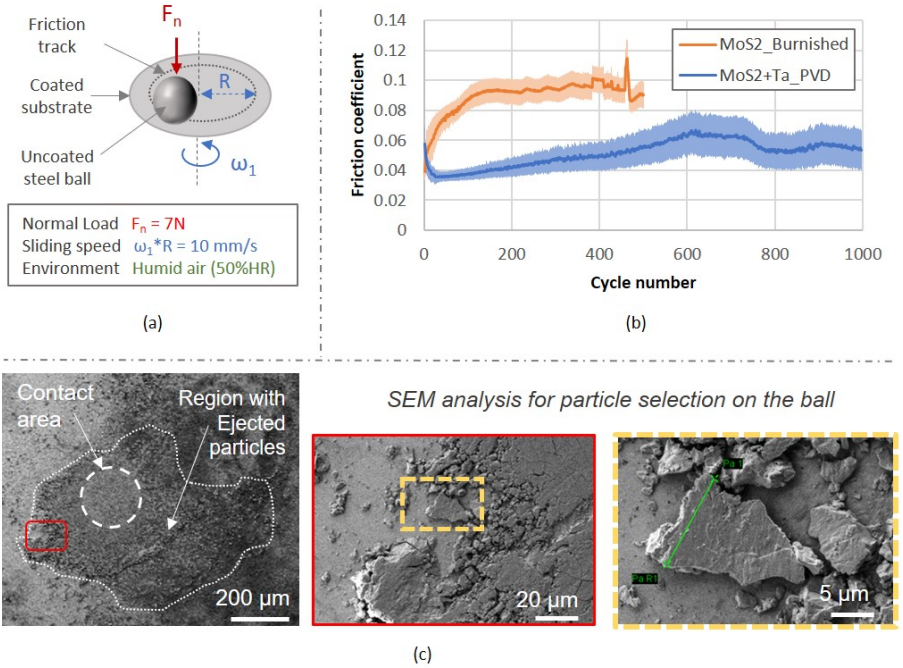

Fig. 1: a- Schematic of the friction test and related contact conditions. b- Friction coefficient with standard deviation (shaded areas) resulting from friction tests with MoS_2 and MoS_2+Ta. c- SEM images of the contact area on the ball and its vicinity, with zoomed-in images to show how particles are distributed and the randomness in sizes, from pure MoS_2 sliding tests.

with layers stacked in a parallel arrangement, Fig. 2(a). In such a configuration, it is agreed that the lubrication properties of MoS_2 are undertaken by the layered nature which offers easy slippage between the basal planes, and consequently low friction. Submitting the pure MoS_2 coating to friction results in third body particles which appear very different from raw material. Although similar in shape to the raw MoS_2 material, the nanolayers disappear to the benefit of a relatively unified, continuous, and more homogeneous microstructured body, Fig. 2(c). This transformation to a third body may have implications for the material mechanical properties, such as changes in its friction behavior, and lubrication performance. The addition of Ta particles significantly alters the structure of MoS_2 [15], which eventually results in the creation of a unique third body with granular microstructure. The MoS_2+Ta third body exhibits nanograins stuck together, forming a cohesive microscale body, Fig. 2(d). As lubrication is undertaken by the third body, and considering the significant differences in morphologies of the 3 types of particles, their mechanical properties are most likely very different, which require individual characterization. Investigating the structural modifications and mechanical responses of the pure MoS_2 third-body

and the granular structure of the MoS_2+Ta third-body leads us to comprehend its potential as an effective friction-reducing material.

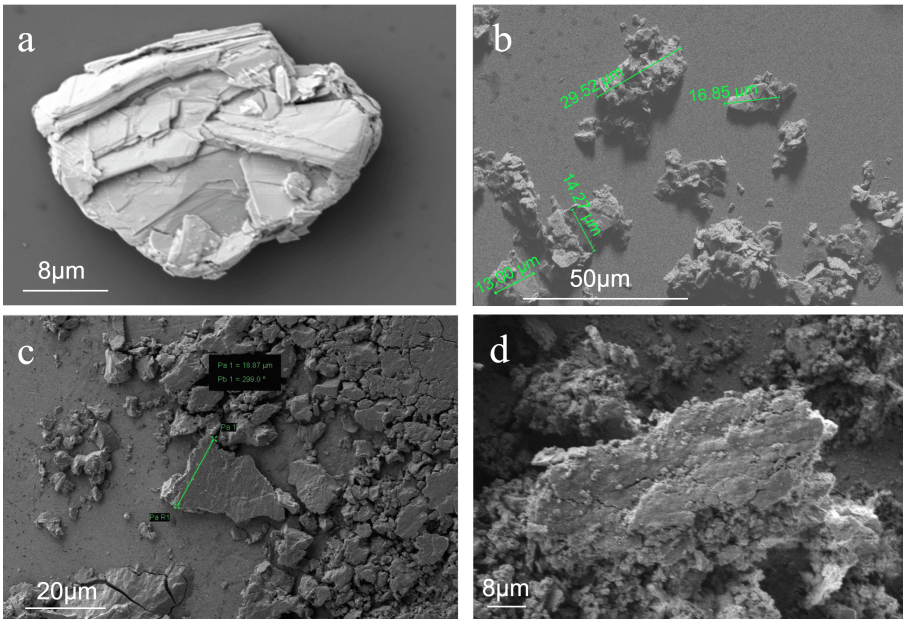

Fig. 2: a- MoS_2 grain, visualizing the nanolayers forming a microparticle. b- Different MoS_2 particles, scaling from 10 to 25 μm before cleaning process. c- Third-body particles created from pure MoS_2. d- Third-body particles created from MoS_2+Ta.

Raw MoS_2 particles also present additional interest for the study. As mentioned earlier, the burnished MoS_2 coating is made from raw MoS_2 commercial powder similar to the one from which particles are extracted. Burnishing consists of gently rubbing the powder on the substrate surface to build up a thin coating that subsequently undergoes friction. Furthermore, the alignment of the layers implies very different in-plane and out-of-plane mechanical properties, which must play an important role in influencing the mechanical response of raw MoS_2 during manipulation and deformation processes. Additionally, the lamellar behavior of raw MoS_2 in the microscale opens up opportunities to explore its unique responses to force application along different orientations, providing complementary information to the existing literature [16, 17] on its mechanical properties.

To quantify the mechanical properties of these different particle structures, force-displacement measurements should be performed in different directions of interest. Through the integration of advanced robotic systems and nanomanipulation techniques within the SEM environment, the objective is to gain insights into the mechanical behavior of these particles under precise, directional, and controlled force application. By characterizing these different particle structures and quantifying their

mechanical properties using the same system, this study aims to provide data for evaluating their performance as third-body materials and their potential applications in reducing friction and energy losses.

2.2 μROBOTEX platform

The μROBOTEX platform used in this study is a system that combines the capabilities of a Scanning Electron Microscope (SEM) with Focused Ion Beam (FIB) and Gas Injection System (GIS) technologies, Fig. 3(a). This powerful platform allows for both additive and subtractive approaches, enabling precise manipulation and fabrication at the microscale and nanoscale [18–20].

The SEM provides high-resolution imaging, to observe and analyze samples at the nanoscale level. The FIB technology complements the SEM by offering the ability to leverage a secondary view with a 54-degree angle at low power and perform material removal and patterning at the microscale with great precision at high power. Additionally, the GIS allows gas injection control, further enhancing the versatility of the platform.

The platform's sample stage offers 5 Degrees of Freedom (DoF), providing high flexibility for positioning and orienting samples during manipulation and analysis. Additionally, a nanopositioner is added and contributes 3 DoF, facilitating precise movements at the nanoscale level for fine manipulation and as attached the sample stage to provide synchronized movement as shown in the kinematic drawing in Fig. 3(b). The micro/nano-positioning SEM robot has 6 DoF, enabling precise and smooth multi-directional, long-ranged movements.

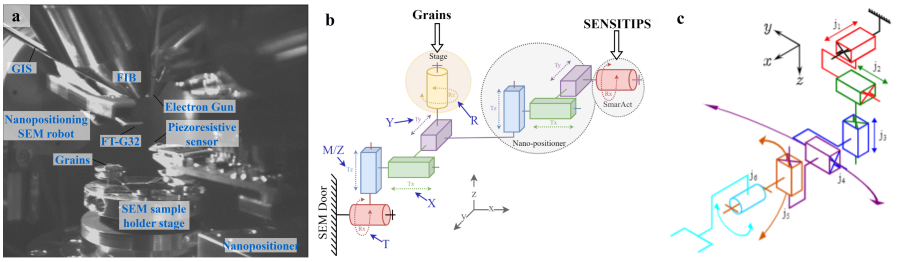

Fig. 3: a- Inside SEM vacuum room, different system view. b- Kinematic diagram showing the 5DoF sample holding stage and the 3DoF nanopositioner attached to it. c- Kinematic diagram of the nanopositioning SEM robot developed at the AS2M department [21].

The combination of these advanced technologies and robots not only enables seamless coordination between imaging, manipulation, and characterization tasks but also serves to minimize the frequency of opening the SEM vacuum chamber. This reduction is crucial to prevent pollution of the samples and particles but also particle loss due to pressure differences and saves valuable time that would otherwise be spent rechecking and restarting the entire system for manipulation confidence purposes.

The kinematic diagram of the robotic systems, Fig. 3(c), anchored inside the vacuum chamber of the SEM platform, illustrates how each component works to achieve the desired tasks. This platform is used to explore the mechanical properties of micrometer-sized 3D grains, enabling insights into friction and lubrication phenomena and advancing nanomanipulation techniques.

2.3 Robotic tools

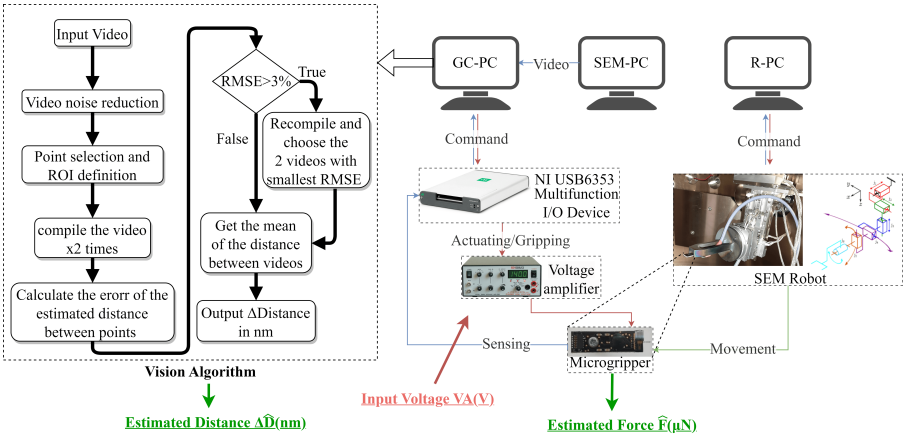

Fig. 4: Micrograpper and vision control systems.

In this study, several robotic tools were used to achieve precise and controlled manipulation of micrometer-sized 3D grains within the SEM environment. The first tool employed was a specialized tip for sample preparation, which allowed for the precise handling and positioning of the grains during the initial stages of the experiments.

A micrograpper (one finger actuated and one instrumented finger, both of capacitive principle, ref. FT-G32, FemtoTools company) has been integrated with the SEM nanopositioning robot providing a seamless and coordinated approach to achieve complex manipulations at the micro and nanoscale levels, Fig. 4. This setup enabled us to grasp, move, and place the grains with accuracy.

To accurately measure the forces exerted on the grains, even during the manipulations, two force-sensing methods were employed. First, the instrumented micrograpper itself provided force-sensing capabilities, allowing for real-time force feedback during the manipulation tasks, reaching up to 70μN. Secondly, a piezoresistive force sensor was integrated on top of the nanopositioner system, as shown in Fig. 5. This sensor provides precise force measurement capabilities with a larger and variable force range, reaching up to 5 mN, and offers a precision of less than 1 μN. This sensor is similar to the one introduced by Komati et al. [22]. To ensure additional safety during the experiments, a SmarAct X-axis rotator was also incorporated into the system, which

raises the piezoresistive force sensor in Z directions while executing fast particle stage movements to evade collisions and fracturing the sensor.

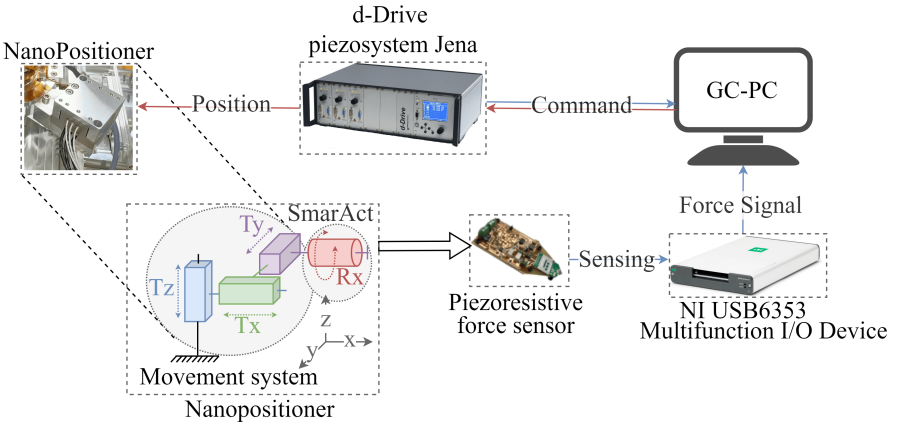

Fig. 5: Piezoresistive sensing system for force measurement application.

The integration of these robotic tools and force-sensing technologies was used for the mechanical categorization of the micrometer-sized 3D particles displayed in the following sections. The combination of automated control and teleoperated manipulation with real-time force feedback allowed a smooth, controlled, and supervised view of forces and deformations experienced by the particles during the handling and manipulation processes.

2.4 Measurement Traceability

Due to the reliance on force measurement data for interpretive analysis, values given by the force sensor must be accurate, meaning near the "true force value". To do so, a preliminary process of "calibration" is needed, where the identification of the relation between the sensor's output and a referenced force applied is calculated. For example, for a force sensor with an output voltage variation ΔU considered as linear with the force applied F, the parameter identified is the sensitivity S in V/N with the formula:

$$F = \frac{\Delta U}{S} \tag{1}$$

Up to now, it is essential to note that there is currently no established standard for force measurement at small scales, despite the growing demand for such standards across various applications. This absence poses a challenge, as many fields require

precise force measurements at small scales to ensure the comparability of obtained results. As highlighted in [23], laboratories are developing their own processes to compensate for this lack, and three primary methods are commonly employed to calibrate force sensors in the context of a tethered robotic system. They all rely on applying a determined reference force along the measured direction of the sensor to be calibrated, assuming the reference force and force estimated by the sensor to be equal. However, this approach induces many parameters influencing the accuracy of the measurement, for example, angles between the two forces, the direction of the relative motion generated to bring the sensors in contact, and drifts induced by ambient conditions changes.

The propagation of these influential parameters to the force measurement is called traceability and results in a confidence interval onto the final force measurement also called force uncertainty [24]. The method chosen to calibrate the piezoresistive sensor involves using a commercial force sensor, a choice made based on a compromise between uncertainty and configuration versatility. It is proposed to analyze the main sources of uncertainty during the calibration process, and their final impact on the force measured by the piezoresistive sensor.

2.4.1 Calibration process

A FemtoTools micro force sensor FT-S270 with a 2,000μN force range shown in Fig. 6(a) is considered as the reference force sensor in this study. To measure the signals from both force sensors, the displacement, and environmental parameters, a precisely synchronized I/O Device at a 100Hz frequency is used.

To create the force, the two test bodies of the piezoresistive sensor and the reference are aligned and approach/retract cycles are controlled. For that, a 3-axis nanopositioner PI-562.3CD with a 200μm travel range is used, paired with its controller PI-E712 in closed-loop control. The motion is a staircase with a maximum position value corresponding to a reference force over 1,200 μN (Fig. 6(b)). The speed of the positioner is set to 1μm/s, the same value used in the mechanical tests. Each level of the staircase lasts for 1 second. The use for this is to calculate an average value of each level, leading to more precision in the identification of the sensor's sensitivity. This identification is calculated by a least squares linear regression, based on the assumption that the sensor used is linear (Fig. 6(c)). To prevent from specific possible behaviors happening around the contact, only values above $10\mu N$ are used for this linear regression.

2.4.2 Uncertainties analysis

The sensitivity of the piezoresistive sensor is identified to be $S = 1.263.10^{-3}$ V/μN which is used in the formula 1. The traceable calibration process of the reference force sensor used is typically documented in [25] and conducts to a global uncertainty of 0.27% of the force measured for the calibrated sensor with a 95% confidence interval. This interval means that any force F measured by this sensor has a 95% to be in the interval $F \pm 0.27\%$. The main source of this uncertainty was the angle consideration at the contact point because it introduces shear stress in the reference force sensor.

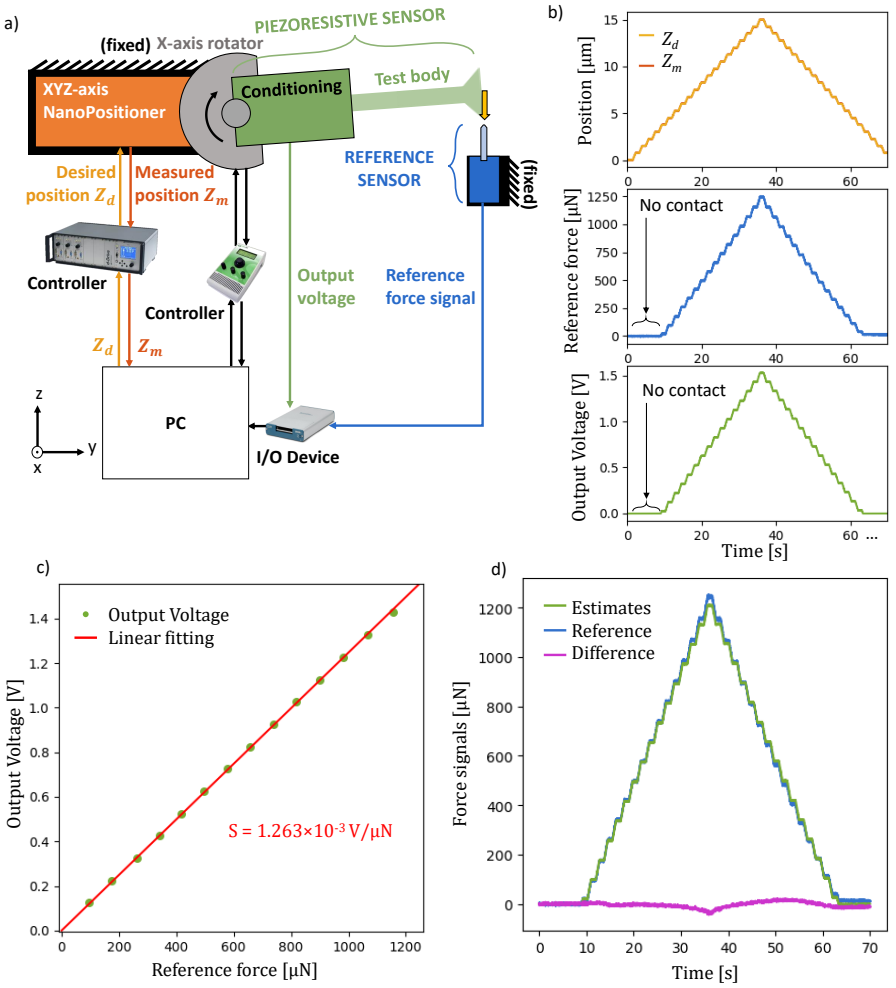

Fig. 6: Calibration process of the piezoresistive micro-force sensor. a) Schematic view of the solicitation setup. b) Time-dependent curves of the position desired, measured, reference force, and output voltage of the piezoresistive sensor. c) Calibration results of the first approach obtaining $S = 1.263.10^{-3}$ V/μN. d) Experimental validation measurements providing the resulting force estimates compared with the reference force applied.

To reduce it, authors analyzed planar and out-of-plane angles effects on the force uncertainty by controlling them. They finally considered a small default of 0.3°. Because no angle control strategy is used in our study, we considered a worst-case of 5° scenario. By using the relation given by [25] between the angles uncertainties in both planes and the propagated force uncertainty, the relative uncertainty of the reference force becomes 3.2% with a 95% confidence interval. This value corresponds

to the force accuracy of the piezoresistive sensor in this configuration and will be the value considered in this paper.

To evaluate the dispersion of the measured values, a statistical study is conducted based on the repetition of approach/retract cycles more than 400 times. Environmental variations such as temperature ($\pm 0.5°C$), hydrometry ($\pm 2\%$) and pressure($\pm 2mbar$) were measured during the test. In these conditions, we considered that the global dispersion uncertainty can be evaluated as the difference between estimated/measured force and reference force (Fig. 6(d)) during every cycle. This difference reaches a maximum absolute value of 35μN when the maximum sensor range is reached i.e. for 1200 μN.

2.5 Vision algorithm

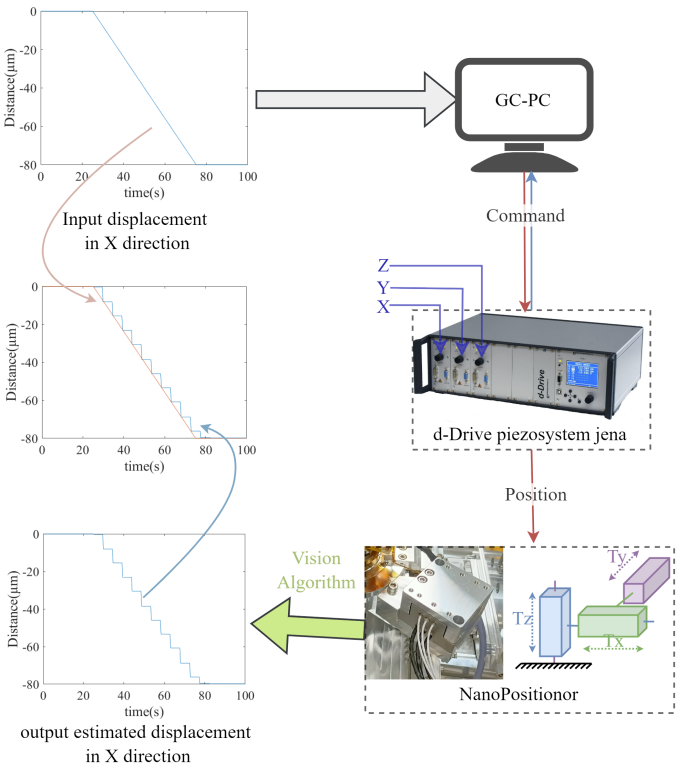

Fig. 7: Vision algorithms behavior detecting changes in the micrometer scale.

This study introduces a vision algorithm designed to assess the deformation of micrometer-sized 3D particles subjected to a force. Leveraging advanced image processing techniques, the algorithm analyzes alterations in particle shape and dimensions, offering valuable insights into their mechanical responses to external forces.

By optimizing the algorithm for Scanning Electron Microscope (SEM) video data, including considerations such as resolution, contrast, and illumination; and integrating it with force sensor measurements, a holistic understanding of particles' physical and visual properties is achieved. The approach enables detailed force-deformation curve generation, exemplified in Fig. 11, shedding light on the nuanced mechanical behavior of particles under varying force conditions. The algorithm's refinement, involving validation and testing, ensures precision by comparing against manual categorization and iteratively adjusting. Integration of the algorithm's results with force sensor measurements enhances the categorization process, offering a comprehensive view of particle characteristics. Video analysis and tracking of multiple points, as depicted in Fig. 4, enable accurate displacement measurements. Robust error mitigation strategies address challenges such as anomalies in scanning speed affecting point tracking, ensuring the reliability of distance estimations.

Tests on the vision algorithm were conducted at different scales to validate its performance under various conditions. In the first validation test, the algorithm demonstrated its reliability in handling larger-scale changes in the micrometer range. A point on the nanopositioner Piezosystem Jena was tracked while applying a linear input spanning 0 to 80 μm (Fig. 7). Despite observed stair-like deviations attributed to SEM scanning speed, the algorithm maintained accuracy.

In the second test, the FT-G32 was utilized to apply a force of 60 μN alongside a rigid glass bead, aiming to evaluate the algorithm's performance at the nanoscale. Quantitative assessments of the minimum force required to induce a 1nm deformation in the glass silica bead were integral to understanding its mechanical behavior. Employing Hooke's Law, the force F was estimated using the formula $F = E \cdot A \cdot \frac{\Delta x}{L}$, where E represents the elastic modulus, A is the cross-sectional area, Δx is the deformation, and L is the original length. Considering $E = 45GPa$, the calculated force was approximately 1.92 N. The application of a force of 60μN alongside the rigid glass bead in experimental tests is insufficient to visualize any notable deformation. The test results of the vision algorithm exhibited minimal drift, with a maximum error of merely 6 nm (Fig. 10). Precautionary measures were implemented during subsequent tests to mitigate rare occurrences of bead slipping. This precision instills confidence in the algorithm's application for subsequent experiments.

3 SAMPLE PREPARATION

The sample preparation and manipulation procedures were essential steps in the study of micrometer-sized 3D particles, raw MoS_2, MoS_2-based third-body, and MoS_2+Ta-based third-body. Initially, raw MoS_2 grains were in a dispersed state, randomly scattered within the workspace, Fig. 2(b). To remediate this problem, we mixed the particles with ethanol (to enable a good dispersion of the particles) and an ultrasonic cleaning bath (to remove the nanograins that could be attached to the main particles of interest), which allowed us to visualize them clearly, Fig. 2(a). However, the third bodies were directly extracted from the friction track vicinity (outside contact area on the sliding ball), and placed on the SEM stage.

To begin the manipulation process, a metalized (Chromium layers by Physical Vapor Deposition) glass probe, refined using the FIB technology, Fig. 8(a), was employed to carefully isolate the individual particles of interest from the surrounding third body materials. Very fine precision is required during this step to ensure that the grains are not damaged or altered during the process.

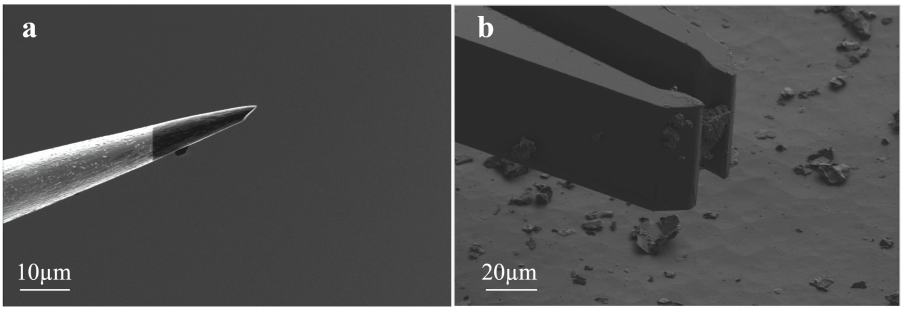

Fig. 8: a- Refined probe using the FIB. b- Manipulation of particles using the micro-gripper.

Once isolated from the surrounding materials, each particle was transferred to a clean silicon wafer substrate by using a force-controlled microgripper for further analysis and manipulation. Then, two different mechanical tests are performed:

1- micro-compression testing using the force-sensing microgripper (Fig. 9(a)). After repositioning the particles appropriately for optimal gripping (particle orientation and position between the fingertips), the compression test is performed without physical contact between the particle and surface, Fig. 8(b). The feasibility of this approach is attributed to the microgripper's design, which incorporates one actuated finger and one sensing finger.

2- micro-compression testing using the piezoresistive force sensor visualized in Fig. 9(c). The particles were positioned to a specific, triangular FIB-formed, gap on the silicon-based support. As such, they are "cornered" to enable compression tests with the piezoresistive force sensor. This approach ensured accurate particle placement, to firmly anchor the particles in place, Fig. 9(b). Throughout this manipulation sequence, the micropositioning SEM robots played a pivotal role in leveraging both the probe and the microgripper, to offer precise control over particle movement, and guaranteeing their accurate relocation for a comprehensive range of testing and analysis purposes.

Several challenges were encountered and addressed to ensure accurate and reliable results. The manipulation of micrometer-sized 3D particles posed unique difficulties, such as dealing with charging effects on the tools within the SEM environment which highlights the importance of grounding all the components of the workspace, and the occurrence of particle attachment to the robotic tools due to various phenomena, Fig. 9. Additionally, the precise positioning of the robotic tools was crucial to avoid unintended damage to the delicate components during the manipulation process. Moreover, the complexity of the 3D particles required careful planning and adaptation of the robotic strategies to achieve successful manipulation.

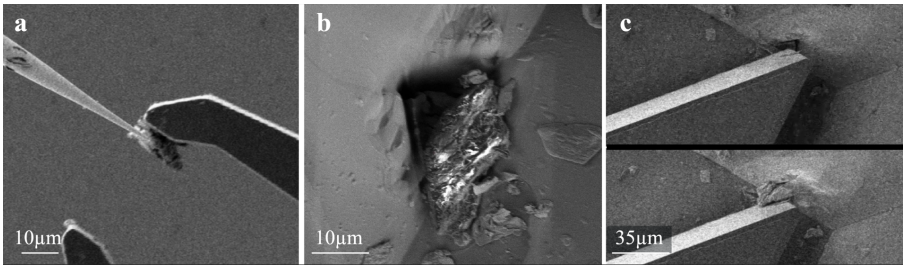

Fig. 9: a- The use of a fixed probe to remove the particle adhered to the gripper. b- MoS_2+Ta third-body positioned into the wall gap for force application. c- View of the piezoresistive force sensor's tip during force applications.

To overcome these challenges and enhance the efficiency of the experiments, automation played an influential role. Automating the manipulation tasks not only saved time but also reduced the risk of human error, ensuring reproducible results, especially for the specific orientation of the force application. The sample preparation and manipulation, coupled with the integration of advanced robotic tools and force-sensing technologies, allowed us to exploration of the micrometer-sized 3D particles' mechanical properties. Moreover, the successful automation of manipulation tasks highlights the potential of robotics in optimizing nanomanipulation processes.

4 Results

The validation of the different robotic systems was an essential step in ensuring the accuracy and reliability of the results. To achieve this, several complementary tests were conducted on the instrumented microgripper and the piezoresistive force sensor. The validation procedures aimed to verify the precision of force measurement, and the overall performance of the robotic tools within the SEM environment, while providing a reference about the behavior of the tools.

4.1 Validation

The validation phase of the microgripper (FT-G32) in its working environment started with essential gripping tests to check its repeatability (commercially available gripper with already established characteristics). By performing gripping actions without any specimen, we evaluated the tool's behavior across multiple trials and verified its reliability for subsequent manipulations. Additionally, the drift of the tool's behavior was examined under steady contact and no contact conditions, providing insights into its sensitivity and accuracy during gripping operations. To establish the accuracy and reliability of the microgripper, solid plain rigid silica glass bead has been used, within the scale of the particles, as reference material, Fig. 10(a). The glass bead served as a benchmark to compare the force response obtained from the gripper with the known properties of the reference material. This comparison allowed to validate the accuracy of the gripper force readings, Fig. 10(c), and assess the performance of the

vision algorithm developed for nanoscale measurements, Fig. 10(b), as nanometric displacement observed (signal noise of SEM measurements for such cases).

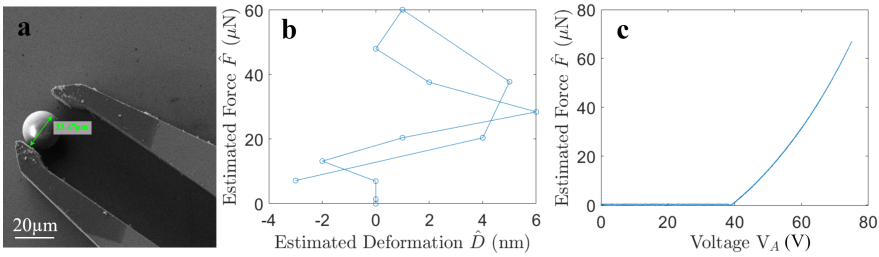

Fig. 10: a- Gripping of a rigid silica bead. b- Exhibited deformation obtained from the vision algorithm. c- Gripper estimated/sensing force when a V_A voltage is applied to its actuator.

Post-experiment validation verified the sensor's stability and ability to maintain accurate force measurements even under challenging conditions during manipulation tasks. An empty test application provided essential baseline data for interpreting force measurements during subsequent particle manipulations. The validation of the sensor demonstrated its reliability and precision, proving its significance as a tool for accurate force analysis during particle manipulation within the SEM environment.

4.2 Characterization of different particles

The vision algorithm allowed to estimate the deformation $\hat{D}$ of the particles during force application using the FT-G32 microgripper, providing details on the mechanical behavior of the different materials, Fig.11.

Fig.11 shows the deformation of the particle during sequential loading (cf. Supplementary Information section). The particle undergoes compression to a specific load, then it is unloaded to zero compression load, reloaded to a higher load, unloading. Deformation under compression at maximum load is shown by the empty circle, and the remaining deformation after unloading but not releasing the particle is shown by the asterisk. The asterisk at $\Delta\hat{D}$ = 0 nm implies fully elastic recovery, and the asterisk at $\Delta\hat{D}$ > 0nm implies plastic remaining deformation. Each circle corresponds to a test performed on the particle in the deformation state at the previous asterisk, i.e the test at 58 μN with MoS_2+Ta third body (Fig.11-particle c.2) is done on a plastically deformed state (previous asterisk at $\Delta\hat{D}$ = 50 nm). The particle is undergoing higher deformation at 58μN than at 70μN. That comes from the fact that the material enters the plastic deformation regime above 40μN. As it deforms, and as the load increases, it eventually reaches a maximum deformation upon compaction. At 58 μN, the material undergoes large plastic deformation (1.2 μm residual deformation after unloading), it hence becomes highly densified and compacted. There is little room left for deformation, even at a higher load (70μN). Such behavior is in line

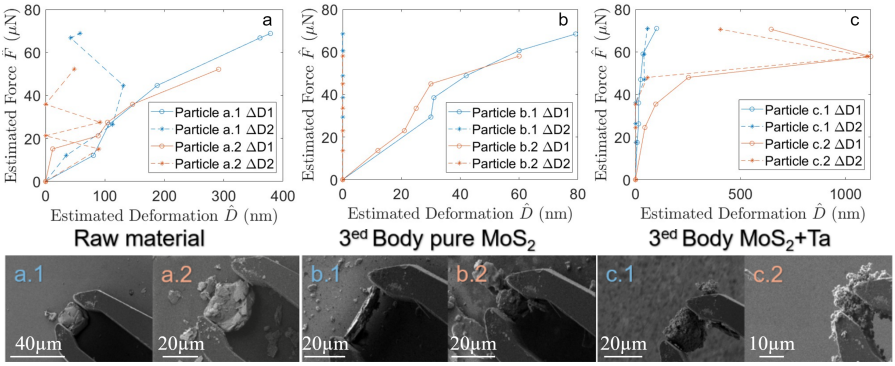

Fig. 11: Estimated force $\hat{F}$ vs deformation $\Delta\hat{D}$ of the different particles.
$\Delta D1$ represents the deformation of the particle a.2 between the initial state (no applied force) and the intermediate state where the desired force is applied.
$\Delta D2$ illustrates the difference in deformation between the initial state and the final state when no force is being applied to the particle anymore.

with the evolution of the force as a function of the estimated deformation of the particle obtained from a compression test performed on a similar particle. Fig.12 allows to visualize the sudden crack events that affected the thickness of the particle and are highlighted by the yellow arrow on instants (b), and (c) after a large deformation. Such events lead to permanent plastic deformation of the particle. The particle, similarly to particle c.2, undergoes large permanent deformation, and upon unloading, only a low elastic recovery of about 100 nm is observed. The second particle, particle c.1, exhibits much lower deformations upon loading. It however demonstrates fully elastic behavior below 40 μN, and an almost fully perfectly plastic behavior above 40 μN compression loading. The change in mechanical response around the 40 μN threshold is relevant to particle c.2.

Contrary to MoS_2+Ta third body particle, which can exhibit significant deformation (up to 1,200 nm) and permanent plastic deformation, the third-body created from pure MoS_2 exhibited very limited deformation of approximately 80nm highlighting its exceptional stiffness (Fig.11). Moreover, it also fully returns to its initial state after force retraction, which demonstrates fully elastic behavior upon compression, in the range of the applied force. Interestingly, it appears that the deformation upon compression exhibits 3 different elastic regimes: one very stiff in the 20 μN to 45 μN force range, which corresponds to 20 nm to 30 nm of deformation. Outside the specified range, the Force vs. Deformation curve exhibits a slope that is at least half of that within the range. However, irrespective of the deformation extent, the material consistently returned to its initial state upon unloading.

When analyzing raw MoS_2 particles, the deformation response of particles a and b are consistent, and a maximum $\Delta\hat{D}$ of nearly 400nm is displayed upon applying a force of 70μN. Although chosen to be displayed, the data points of 18 μN (particle a.2) appear not relevant considering that unloading the contact results in 80 nm shrinkage of the particle. These outliers removed deformation upon loading and follow similar

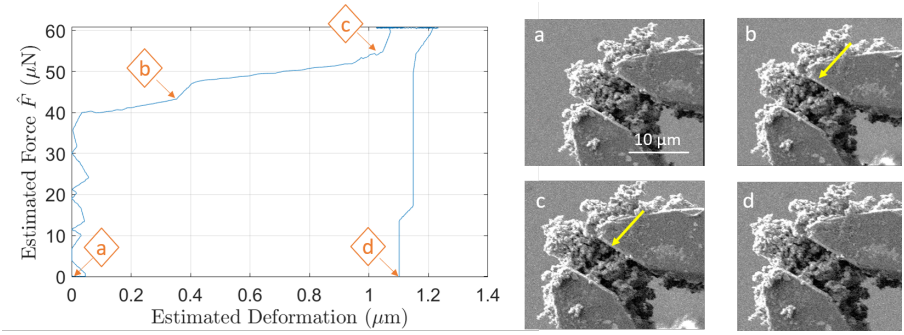

Fig. 12: Compression test of MoS_2+Ta third body particle plotted as Estimated force $\hat{F}$ vs estimated deformation of the particle; images (a) to (d) are images of the particle at different stages of the compression test. Yellow arrows are pointing toward the main crack.

trends in terms of both variations and values (force$\hat{F}$ and $\Delta\hat{D}$). When increasing the compressive loading, both particles demonstrate alternatively either large or small (even null sometimes) permanent deformation. That shows elastic, elastic-plastic, and fully plastic behaviors, but those happen alternatively and successively upon loading. To identify if plastic deformation occurs progressively or suddenly, force$\hat{F}$ has been plotted against voltage V_A (Fig.13). The response is intriguing considering that upon unloading a constant force$\hat{F}$ is maintained before unloading (Force wise) eventually occurs. Force variations during unloading appear very similar to the loading variations. Both loading to the next compressive force, and subsequent unloading, follow the same pattern as the previous loadings, which would support fully elastic behavior. Only the vision algorithm allowed to evaluate the existence of plastic deformation. The cyclic loading demonstrates that the response of the raw MoS2 consistently follows the same trends, even after minor plastic deformation, which questions the occurrence of a possible reconfiguration of the stacking of the layer comprising the particle. This behavior is observed for all raw MoS_2 particles tested, it is hence reproducible. In the study [17] it is shown that when the stacking of MoS_2 basal planes comprises above 20 basal planes (nearly 20nm in thickness), the deformation behavior under in-plane compressive loading resulted in sudden kink formations and that the mechanism is almost fully reversible as most kinks disappear upon unloading. The nano-sheet (stack of the 20 basal planes) fully unfolds to get back in place. Further, in-depth analyses are needed to fully understand the underlying mechanisms leading to the observed behaviors.

The results from the microgripping experiments have been compared with those obtained with the piezoresistive sensor, which relied on applying a compressive force on particles "cornered" in place on a wafer patterned with angular holes. Upon compressive loading until failure, similar behaviors are observed:
(i) Very stiff for third body particles from MoS_2 coating with no crack events.
(ii) Plastic behavior of MoS_2+Ta based third body particle, the first cracks event appearing below, but close to, 100 μN. Multiple events then follow until the particle

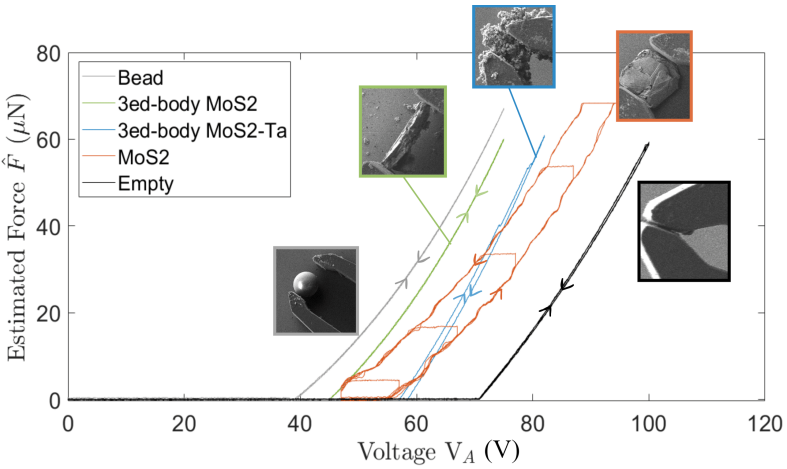

Fig. 13: Estimated force $\hat{F}$ vs input voltage V_A of the microgripper, empty and rigid bead gripping to set references, then lateral gripping on raw MoS_2, the third-body created by MoS_2 and the third-body created from MoS_2+Ta.

gradually collapses and the piezosensor tip gets into contact with the wafer, at $N_pP = 78\mu m$. After that $\hat{F}$ increases linearly, which reflects the stiffness of the SensiTip. (iii) Occurrence of sudden crack or reconfiguration events leading to a sudden and moderate drop of force $\hat{F}$ at $N_pP = 74\mu m$ for raw MoS2 particle. Following the moderate drop, forces increase until the complete fracture of the particle at $N_pP = 77\mu m$. The shape of the force increase and the sudden moderate force drop correlate well with the experiment of [17] who showed similar increase and drop when kink forms within the MoS2 planes.

That emphasizes the need to pursue investigations regarding the mechanisms leading to those sudden events. Moreover, the first significant event occurs at 50 μN, which is in line with the range of force where significant plastic deformation starts to be detected during the compressive testing using the microgripper Fig.11.

In the context of lubrication, these observations appear to confirm the assumption that lubricity from MoS_2-based coatings is achieved through the creation of third bodies that demonstrate ductile behavior (plastic flow) inside the interface [15, 26]. In the presented case, pure MoS_2-based coating failed to lubricate the contact earlier and provided higher friction, which is in line with the fact that the third body is very rigid and does not demonstrate plastic behavior. The MoS_2+Ta coating, on the other hand, succeeded in lubricating and provided low friction, which is in line with the elastic-plastic behavior identified and the occurrence of large permanent deformation upon compression, even at low loads.

The comparison of results obtained from the vision algorithm hence provides a first quantitative evaluation of the force/deformation mechanical response of the 3rd body materials directly extracted from the friction tracks. The study provides unprecedented

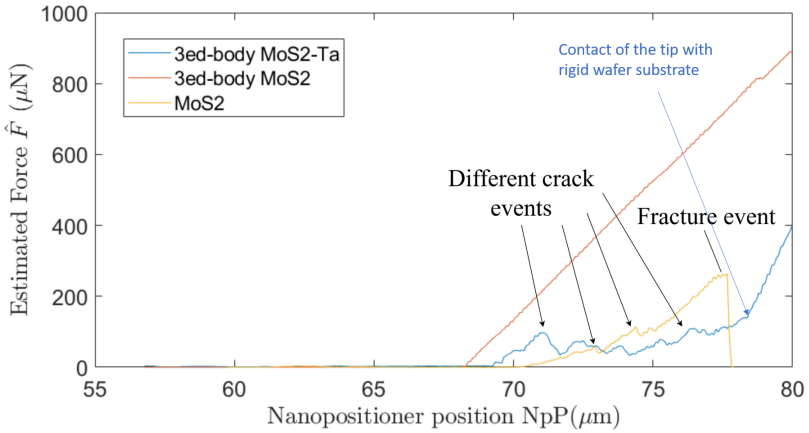

Fig. 14: Estimated force $\hat{F}$ from the piezoresistive sensor on the different particles, and observation of multiple crack events mainly from the raw MoS_2 and the third-body formed from MoS_2+Ta; and the fracture of the raw MoS_2.

information on the mechanical properties of the third bodies, combined with the friction performances. The varying deformation responses and recoverability observed in the different materials shed light on their distinct mechanical characteristics.

5 CONCLUSIONS

The present study presents the challenges and achievements in the manipulation and characterization of micrometer-sized particles with 3D structures having different geometries and complex internal sub-micrometer structures. Throughout the study, several complementary commercial and lab-developed micro and nanomanipulation tools have been integrated within the vacuum SEM chamber environment. This integration allowed us to conduct precise and automated force-displacement measurements accompanied by carefully devised robotic strategies to enable the whole process from micron-sized particle selection, manipulation, and characterization in-situ SEM. The characterization includes highly controlled compressive testing (in terms of force and displacement) monitored in-situ by the SEM. Through an in-house developed vision algorithm, particle deformation upon compressive has been determined. First, quantified results have thus been obtained, with compression forces typically lying in the range of a few micro-Newtons to several hundreds of micro-Newtons, and deformations lying in the range of 10 nm to above 1 μm. Two complementary tools have been operated: a commercial microgripper and an in-house developed piezosensor. They have been calibrated in-situ and combined with nanopositioning devices to ensure the reliability and versatility of the resulting in-situ testing platform.

A case study on the evaluation of mechanical properties of tribological materials has been conducted. It focuses on 3 distinct MoS_2 based particles: 2 third body wear

particles generated during friction from 2 different lubricated contacts, and one pristine purely crystalline particle. The three materials demonstrated different mechanical responses under force application. The pure MoS_2-based third-body exhibited the highest stiffness and purely elastic behavior in the range of forces explored, while the third-body formed from MoS_2 and Ta displayed an elastic-plastic behavior with cracks and large plastic deformation occurring at low forces (around 50 μN). These findings provide unprecedented quantitative information into the mechanical properties of these materials and how they correlate with their lubrication efficiency. Beforehand, such correlation only relied on qualitative assumptions. The study hence offers possibilities for better understanding their role in friction, which paves the way for further application in various engineering scenarios, and fundamental studies on the role of the mechanical properties of third bodies in the tribological behavior of materials. These initial results show promising coherence and open avenues for further exploration and exploitation. Better-controlled experiments with perfectly known regular-shaped geometries are needed to complement measures on unmodified particles and to pursue the quantification of the mechanical properties of the particles using the methodology developed here. The 3D geometry of each and every unmodified particle tested must also be known to extract stress/strain relationships. Finally, a statistical approach is mandatory considering the dispersion in the particles morphologies. Future investigations, though combined studies with numerical modeling for example [27], will also contribute to a deeper understanding of the underlying mechanisms and potential applications of these unique nanoscale structures.

Overall, this article's primary contribution lies in the first quantified results on MoS_2 particles and their third-bodies, showcasing the utilization of advanced tools and robotics for simultaneous manipulation and characterization of materials with complex 3D structures at the micro and nanoscales.

Acknowledgement

This work has been partially funded by the DYNABOT Project under the contract ANR-21-CE10-0016, by Région Bourgogne Franche-Comté, the EIPHI Graduate School (ANR-17-EURE-0002) and the French RENATECH and ROBOTEX networks (TIRREX ANR-21-ESRE-0015) through their FEMTO-ST technological facilities MIMENTO and CMNR. Authors are thankful to Pierre Roux for the fabrication of components, they are also thankful to the French Space Agency (CNES) for authorizing the use of third-body particles originating from specific tribological tests.

Declarations

Competing interests

This declaration is not applicable.
The authors have no competing interests, or other interests that might be perceived to influence the results and/or discussion reported in this paper.

Authors' contributions

R.H., C.C., J.-Y.R., and G.C. designed the Robotic system. R.H. and J.-Y.C. performed the manipulations. V.R., J.A., and C.C. developed the piezoresistive sensor. G.C. provided the studied material in its different states. R.H. and F.M. developed the electronic connections. O.L., F.M., J.-Y.R., and R.H. developed the control interface of the robotic system. G.C. verified and analyzed the data. R.H., G.C., C.C., and V.R. drafted the manuscript. R.H. prepared figures 2-6,8-12,14,15, G.C. prepared figures 1,13, and V.R. prepared figure 7. All authors have access to all the data and revised and approved the final manuscript.

Funding

This work has been partially funded by the DYNABOT Project under the contract ANR-21-CE10-0016, by Région Bourgogne Franche-Comté, the EIPHI Graduate School (ANR-17-EURE-0002) and the French RENATECH and ROBOTEX networks (TIRREX ANR-21-ESRE-0015) through their FEMTO-ST technological facilities MIMENTO and CMNR.

Availability of data and materials

This declaration is not applicable.

References

[1] Zimmermann, S., Haenssler, O.C., Fatikow, S.: Manipulation of liquid metal inside an SEM by taking advantage of electromigration. Journal of microelectromechanical systems **28**(1) (2019). https://doi.org/10.1109/jmems.2018.2878320

[2] Shi, C., Luu, D.K., Yang et al., Q.: Recent advances in nanorobotic manipulation inside scanning electron microscopes. Microsystems and Nanoengineering **2**(1) (2016). https://doi.org/10.1038/micronano.2016.24

[3] Clévy, C., Sauvet, B., Rauch et al., J.-Y.: In-situ versatile characterization of carbon nanotubes using nanorobotics. In: International Conference on Manipulation, Automation and Robotics at Small Scales, pp. 1–6 (2019). https://doi.org/10.1109/MARSS.2019.8860970

[4] Berthier, Y.: Experimental evidence for friction and wear modelling. Wear **139** (1990). https://doi.org/10.1016/0043-1648(90)90210-2

[5] Godet, M.: The Third-Body Approach: a Mechanical View Of Wear. Wear **100** (1984). https://doi.org/10.1016/0043-1648(84)90025-5

[6] Holmberg, K., Erdemir, A.: Influence of tribology on global energy consumption, costs and emissions. Friction **5**(3), 263–284 (2017). https://doi.org/10.1007/s40544-017-0183-5

[7] Wang, M., Yang, Z., Chen, T., Sun, L., Fukuda, T.: Motion control of nanomanipulation platform based on feedforward compensation inside sem. In: IEEE International Conference on Nano/Micro Engineered and Molecular Systems, pp. 370–374 (2019). https://doi.org/10.1109/NEMS.2019.8915647

[8] Qu, J., Wang, R., Pan, P., Du, L., Mi, Z., Sun, Y., Liu, X.: An sem-based nanomanipulation system for multiphysical characterization of single ingan/gan nanowires. IEEE Transactions on Automation Science and Engineering **20**(1), 233–243 (2023). https://doi.org/10.1109/TASE.2022.3146486

[9] Michelson, A., Flanagan, T.J., Lee, S.-W., Gang, O.: High-strength, lightweight nano-architected silica. Cell Reports Physical Science **4**(7) (2023). https://doi.org/10.1016/j.xcrp.2023.101475

[10] Adam, G., Boudaoud, M., Reynaud, V., Agnus, J., Cappelleri, D.J., Clévy, C.: An overview of microrobotic systems for microforce sensing. Annual Review of Control, Robotics, and Autonomous Systems **7** (2024). https://doi.org/10.1146/annurev-control-090623-115925

[11] Govilas, J., Guicheret-Retel, V., Clévy, C., Placet, V., Amiot, F.: Introducing compression platen misalignment in single fiber transverse compression analytical models. Journal of Materials Science **58**(42), 16336–16343 (2023). https://doi.org/10.1007/s10853-023-09042-w

[12] André, A.N., Lehmann, O., Govilas, J., Laurent, G.J., Saadana, H., Sandoz, P., Gauthier, V., Lefèvre, A., Bolopion, A., Agnus, J., *et al.*: Automating robotic micro-assembly of fluidic chips and single fiber compression tests based-on xytheta visual measurement with high-precision fiducial markers. IEEE Transactions on Automation Science and Engineering (2022). https://doi.org/10.1109/TASE.2022.3218686

[13] Komati, B., Clévy, C., Lutz, P.: Sliding mode impedance controlled smart fingered microgripper for automated grasp and release tasks at the microscale. In: International Precision Assembly Seminar, pp. 201–213 (2018). https://doi.org/10.1007/978-3-030-05931-6_18. Springer

[14] Holmberg, K., Matthews, A.: Coatings Tribology - Properties, Mechanisms, Techniques and Applications in Surface Engineering vol. 53, 2nd edn. (2009). https://doi.org/10.1016/0043-1648(84)90025-5

[15] Serles, P., Nicholson, E.M., Tam, J., Barri, N., Chemin, J., Wang, G., Michel, Y., Singh, C.V., Choquet, P., Saulot, A., Filleter, T., Colas, G.: High Performance Space Lubrication of MoS2 with Tantalum. Advanced Functional Materials **32**(20), 2110429 (2022). https://doi.org/10.1002/adfm.202110429

[16] Sahoo, R.R., Math, S., Biswas, S.: Mechanics of Deformation under Traction and Friction of a Micrometric Monolithic MoS2 Particle in Comparison with

those of an Agglomerate of Nanometric MoS2 Particles. Tribology Letters **37**(2) (2009). https://doi.org/10.1007/s11249-009-9504-9

[17] Tang, D.-M., Kvashnin, D.G., Najmaei, S., Bando, Y., Kimoto, K., Koskinen, P., Ajayan, P.M., Yakobson, B.I., Sorokin, P., Lou, J., Golberg, D.: Nanomechanical cleavage of molybdenum disulphide atomic layers. Nature Communications **5**(1) (2014). https://doi.org/10.1038/ncomms4631

[18] Benouhiba, A., Wurtz, L., Rauch, J.-Y., Agnus, J., Rabenorosoa, K., Clévy, C.: Nanorobotic structures with embedded actuation via ion induced folding. Advanced Materials **33**(45), 2103371 (2021)

[19] Lei, Y., Clévy, C., Rauch, J.-Y., Lutz, P.: Large-Workspace Polyarticulated Micro-Structures Based-On Folded Silica for Tethered Nanorobotics. IEEE Robotics and Automation Letters **7** (2022). https://doi.org/10.1109/lra.2021.3118470

[20] Rauch, J.-Y., Lehmann, O., Rougeot, P., Abadie, J., Agnus, J., Suarez, M.A.: Smallest microhouse in the world, assembled on the facet of an optical fiber by origami and welded in the microRobotex nanofactory. Journal of vacuum science and technology **36**(4) (2018). https://doi.org/10.1116/1.5020128

[21] Lei, Y.: Nanorobotic Origami Unfolded at the Tip of Optical Fiber (2023, PhD thesis dissertation, Bourgogne Franche-Comté University)

[22] Komati, B., Clévy, C., Lutz, P.: High bandwidth microgripper with integrated force sensors and position estimation for the grasp of multistiffness microcomponents. IEEE/ASME Transactions on Mechatronics **21**(4), 2039–2049 (2016). https://doi.org/10.1109/TMECH.2016.2546688

[23] Adam, G., Boudaoud, M., Reynaud, V., Agnus, J., Cappelleri, D.J., Clévy, C.: An overview of microrobotic systems for microforce sensing. Annual Review of Control, Robotics, and Autonomous Systems **7**(1), (2024). https://doi.org/10.1146/annurev-control-090623-115925

[24] JCGM: Évaluation des données de mesure - Guide pour l'expression de l'incertitude de mesure. https://www.bipm.org/fr/committees/jc/jcgm/publications (2008). https://www.bipm.org

[25] Marti, K., Wuethrich, C., Aeschbacher, M., Russi, S., Brand, U., Li, Z.: Microforce measurements: a new instrument at METAS. Meas. Sci. Technol. **31**(7), 075007 (2020). https://doi.org/10.1088/1361-6501/ab79c7. Accessed 2023-10-17

[26] Colas, G., Saulot, A., Godeau, C., Michel, Y., Berthier, Y.: Decrypting third body flows to solve dry lubrication issue – MoS2 case study under ultrahigh vacuum. Wear **305**(1-2), 192–204 (2013). https://doi.org/10.1016/j.wear.2013.06.007

[27] Colas, G., Pajovic, S., Saulot, A., Renouf, M., Cameron, P., Beaton, A., Gibson, A., Filleter, T.: Adhesion measurements in mos2 dry lubricated contacts to inform predictive tribological numerical models: Comparison between laboratory-tested samples and ball bearings from the niriss mechanism. ESMATS (2017)

Supplementary Information

Fig.15 shows the test sequence corresponding to multiple loading compression tests using the Ft-G32 microgripper, which is referred to as sequential loading in the main body of the manuscript. The input signal is the voltage. The gripper is closed up to step #1, which corresponds to gripping the particle without compressing it. At this step, the particle is held but not compressed, i.e load is equal to 0 μN. This provides the particle's initial size. Voltage is then increased to step#2, which results in a force and deformation state. Voltage is maintained constant, as well as both the load and the deformation in the present case. Neither viscoelasticity nor viscoplasticity have been observed. The deformation under compression (delta D1) is hence measured. Then the particle is unloaded to return to zero load (step#1), where again the particle size (delta D2) is measured. If the size is equivalent to the size at the previous loading step, then the plastic deformation is null; if it is different, then the particle has deformed and the deformation is the difference between the two sizes. In this way, the resulting deformation of each loading and unloading step is evaluated. The total plastic deformation is the sum of the deformations measured at each step.

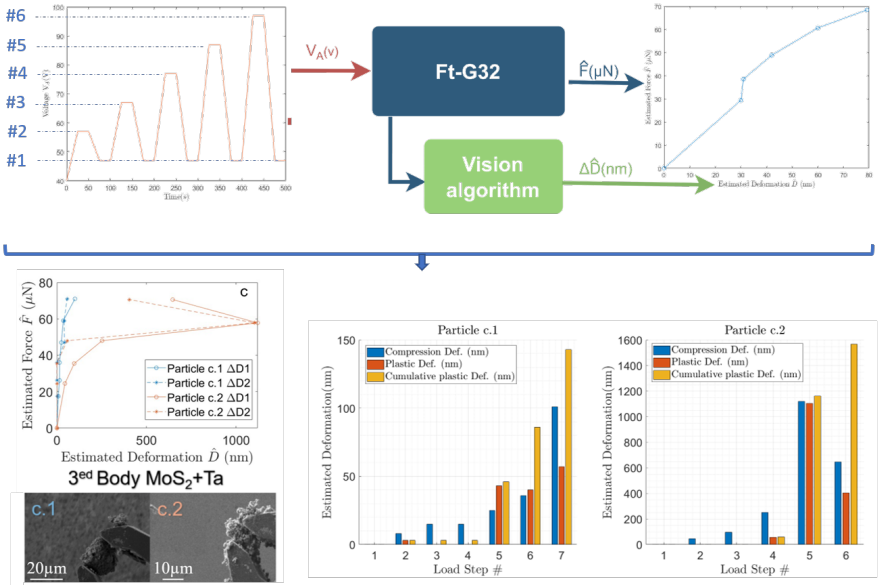

Fig. 15: Test sequence using the Ft-G32 micro-gripper (a) and the resulting data (b) plotted in two different ways: Estimated force $\hat{F}$ vs. Estimated Deformation $\hat{D}$ as it is presented in the main body of the paper, and Estimated deformation upon compression and after unloading for each loading step. Cumulative deformation of the particle is also presented.